Thermal, Structural, and Inflation Modeling of an Isotensoid Supersonic Inflatable Aerodynamic Decelerator

Brandon P. Smith, Ian G. Clark, and Robert D. Braun
Daniel Guggenheim School of Aerospace Engineering
Georgia Institute of Technology
270 Ferst Drive
Atlanta, GA 30332-0150
404-894-7783
bpsmith@gatech.edu

Abstract—Near-term missions to Mars may not be possible with current deployable decelerator technology. This possibility becomes a certainty for the more distant human-precursor missions. Inflatable Aerodynamic Decelerators (IADs) are a candidate technology that may provide the needed drag augmentation to enable these much heavier missions. The attached isotensoid is one of the IAD configurations favored for application at Mars. Assessing the isotensoid's technical feasibility for Mars missions requires several performance models capable of providing reasonably accurate predictions of key design parameters. This paper describes engineering-level models derived from past isotensoid technology development efforts that have been modified or improved for the problem at hand. Easily implemented models of the isotensoid inflation history, aerothermodynamic environment, and thermostructural performance are described.[1][2]

Engineering models are presented for estimating internal pressure and drag during inflation, aerothermal heating on the fabric, stresses throughout the structure, and in-depth fabric temperatures. The models are applied to a reference mission similar to the Mars Science Laboratory (MSL) employing a Supersonic IAD (SIAD) at Mach 5. Thermostructural analysis is presented to show a method for selecting suitable materials capable of performing in the predicted aerothermal environment under the predicted load.

The inflation model is validated with empirical data from Viking-era ground tests. Aerothermal analysis shows that a peak convective heat rate of 1.25 W/cm^2 can be expected across the isotensoid fabric. Stresses are computed for minimum gauge materials, and the transient temperature response of the fabric and thermal coating is computed. Nomex, Kevlar, and Vectran materials are considered. Material tenacity retention at elevated temperatures is considered. Vectran is recommended for the isotensoid fabric due to its adequate thermostructural performance, favorable abrasive properties, and flight heritage as an inflatable structure.

TABLE OF CONTENTS

1. INTRODUCTION

Inflatable Aerodynamic Decelerators (IADs) are a promising technology for greatly increasing performance of entry probes at Mars and other planetary atmospheres. NASA and the Department of Defense have been the main proprietors of this technology through a sporadic development history spanning fifty years. The technology reached a pinnacle during the mission planning phases of the Viking, Pioneer Venus, and Galileo missions, and modern efforts have focused on building on this extensive historical knowledge base [1]. IADs have proven technical feasibility far beyond the proven flight envelope of the disk-gap-band parachute, but they have never been tested in a relevant environment at their intended scale. The attached isotensoid Supersonic Inflatable Aerodynamic Decelerator (SIAD) is one of the favored configurations for high-mass missions to Mars. This geometry consists of an inflatable textile envelope designed for uniform fabric stress in both principle directions and is augmented with meridional cords for fabric load relief. NASA, industry, and academia are currently developing test and analysis techniques to mature this and other IAD configurations.

The flexible nature of inflatable structures and the extreme operating environment make high-fidelity performance analysis difficult during preliminary design. This paper builds on previous literature by presenting simple methods for computing several useful engineering quantities for analysis of attached isotensoids: drag and internal pressure histories during inflation, aerothermodynamic heating on the isotensoid fabric, peak fabric and cord stresses, and fabric temperature profiles. The models are described in detail and validated using analytic methods or experimental data where available.

Presented models are applied to a reference mission similar to the Mars Science Laboratory (MSL). The results are estimates of key quantities that must be known early in the design process for purposes of evaluating feasibility of SIAD configurations, identifying important sensitivities, and informing design of ground and flight tests. One historical material (Nomex) and two modern materials (Kevlar and Vectran) are considered for the SIAD structure. Design recommendations are made based on the thermostructural results and packaging considerations.

2. REFERENCE MISSION

This analysis considers the atmospheric deceleration of a blunt-body aeroshell with an attached isotensoid SIAD. The attached isotensoid, shown notionally in Figure 1, is one of the SIAD configurations being studied for atmospheric deceleration within the planetary exploration community. The isotensoid geometry is characterized by a fabric envelope attached to the rigid aeroshell at shoulder and backshell locations. Ram-air inlets located on the fabric envelope provide the required inflation gas. Some isotensoid configurations include an extra "burble fence" located at the SIAD shoulder. This feature provides uniform flow separation and must be included for stable subsonic flight.
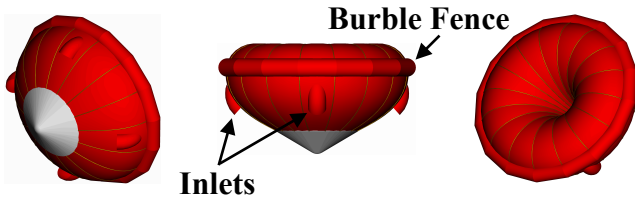

Figure 1 – Attached isotensoid SIAD.

System studies show that SIADs provide the most trajectory benefits at Mars when deployed at Mach 4-6 between 10 and 20 km [2]. This analysis considers a nominal SIAD deployment at Mach 5. The assumed deployment dynamic pressure of 4 kPa is conservative for this range of altitudes. A cross-sectional view of the aeroshell and deployed SIAD is shown in Figure 2 with coordinates of the identified locations listed in Table 1. The isotensoid is sized to provide approximately four times the supersonic drag area, $C_D A$, of the MSL aeroshell, or 105 m^2. This yields an attached isotensoid with a diameter of 11 m.

Table 1 – Coordinates of attached isotensoid features.

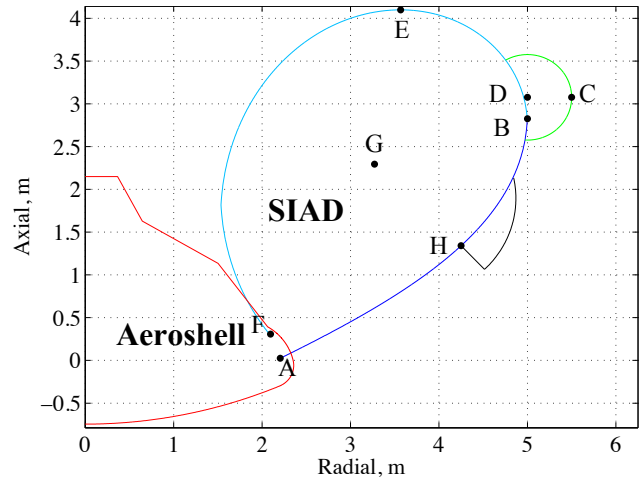| Point	Definition	Radial (m)	Axial (m)
A	Front Attachment Point	2.21	0.0250
B	Maximum Isotensoid Radius	5.00	2.83
C	Maximum Total Radius	5.50	3.08
D	Burble Fence Origin	5.00	3.08
E	Maximum Height	3.57	4.10
F	Rear Attachment Point	2.10	0.308
G	Centroid of SIAD	3.28	2.30
H	Inlet Attachment Point	4.25	1.34

Figure 2 – Profile of aeroshell with supersonic attached isotensoid (coordinates provided in Table 1).

3. INFLATION MODEL

This section provides a description of a mathematical model for predicting the inflation of an attached isotensoid SIAD. Specifically, the model provides a means for estimating the rate of inflation of an isotensoid employing ram-air inlets in terms of the rate of internal pressure and drag area increase. These relations are needed for evaluating the trajectory implications of SIAD deployment and computing the design stresses in the isotensoid materials. Primary inputs to the model include the freestream conditions, volume of the SIAD, and area of the ram-air inlets. The model builds on prior inflation models available in the literature [3][4] and relies predominantly on isentropic flow relations.

The process of isotensoid inflation is broken into three main phases (inlet deployment, volume rise, and pressure rise) delineated by four events. The events are as follows:

Start of Inflation, t_0: This marks the initiation of the inflation process. At this time the isotensoid is pushed out from where it is stored and the fabric is exposed to the freestream. The event would likely be represented by the firing of a small gas generator and the separation of any cover panels used to protect the SIAD during entry. The gas generator is used to provide a small initial pressurization of the SIAD that would be sufficient to expose the ram-air inlets to the oncoming flow.

Inlets in Freestream, t_{if}: At this point the ram-air inlets are exposed to the freestream and the SIAD begins inflating in earnest. Early on in the inflation process the SIAD has insufficient internal pressure to overcome freestream forces and thus the isotensoid begins to inflate aft of the entry vehicle. This inflation process takes the form of a constant pressure process in which ingested air is used to strictly raise the volume of the SIAD. Because the SIAD is expanding into the aft region of the entry vehicle, the

internal pressure is assumed to be equal to the base pressure, P_b.

Full Volume, t_{fv}: At this point the SIAD has expanded as much into the aft regions of the entry vehicle as possible without extending past the shoulder of the vehicle. For modeling purposes, it is assumed that the SIAD has achieved a volume the same as the fully deployed volume. This marks the end of the constant pressure phase of inflation and subsequently air ingested is used to begin increasing the pressure so as to push the SIAD out beyond the shoulders of the entry vehicle.

Full Pressure, t_{fp}: Inflation is assumed to end once the SIAD has reached 99% of the maximum inflation pressure value (either the freestream stagnation pressure or the stagnation pressure behind a normal shock).

Internal Pressure Model

The internal pressure model begins once the inlets are exposed to the freestream, at time t_{if}. The internal pressure of the isotensoid is governed by the mass flow rate into the SIAD via the ram-air inlets and the mass flow rate out of the SIAD due to the porosity of the canopy. Calculations of both flow rates are dependent on whether the flow is choked.

Freestream Calculations—Several parameters dependent on the freestream conditions are required for subsequent calculations. Equations for these are as follows:

$$T_0 = T_\infty \left[1 + \frac{\gamma - 1}{2} M_\infty^2 \right] \tag{1}$$

$$P_{0_1} = P_\infty \left[1 + \frac{\gamma - 1}{2} M_\infty^2 \right]^{\gamma/(\gamma-1)} \tag{2}$$

$$P_{0_2} = P_\infty \left[\frac{\gamma + 1}{2} M_\infty^2 \right]^{\gamma/(\gamma-1)} \left[\frac{\gamma + 1}{2\gamma M_\infty^2 - (\gamma - 1)} \right]^{1/(\gamma-1)} \tag{3}$$

where Equation (1) defines the freestream stagnation temperature, T_0, Equation (2) defines the freestream stagnation pressure, P_{0_1}, and Equation (3) defines the stagnation pressure behind a normal shock, P_{0_2}. T_∞ is the freestream static temperature, P_∞ is the freestream static pressure, M_∞ is the freestream Mach number, and γ is specific heat ratio at Mars ($\gamma \approx 1.3$). Note that Equation (3) is only valid for flight Mach numbers greater than one. For Mach numbers less than one, Equation 4 below should be used for the value of P_{02}. The reason for this is that in later calculations, P_{02} will be used as the value of the maximum internal pressure.

$$P_{0_2} = P_{0_1} \tag{4}$$

The pressure at the base of the isotensoid, P_b, is calculated using an empirical relation [3] as follows:

$$C_{p_b} = \frac{-1}{M_\infty^2 + 0.7}$$

$$P_b = P_\infty - \left(\frac{1}{M_\infty^2 + 0.7} \right) \frac{\gamma}{2} P_\infty M_\infty^2 \tag{5}$$

where C_{p_b} is the base pressure coefficient. Note that Equation (5) is based on supersonic flow. However, an examination of data from recent transonic testing of blunt bodies indicates that the equation can be useful at lower Mach numbers so long as a lower bound of $C_{pb} \sim -0.4$ is enforced. Prior codes have needed to use a constant value of base pressure due to numerical stability issues. However, this depends on the numerical methods used. Keeping the value constant is not thought to be an issue because the value does not change very quickly with Mach number and furthermore the Mach number is unlikely to change significantly during a typical inflation.

Inlet Flow Rate—Calculating the mass flow rate into the isotensoid, $\dot{m}_i$, via the ram-air inlets requires first determining if the flow is choked at the inlet. Thus, two relations are required with a conditional statement as follows:

$$\text{if } \frac{P_i}{P_{0_2}} \leq \left(1 + \frac{\gamma - 1}{2} \right)^{\gamma/(1-\gamma)}$$

$$\dot{m}_i = C_{d_i} \eta_i A_i P_{0_2} \left[\frac{\gamma}{RT_0} \left(\frac{2}{\gamma + 1} \right)^{\frac{\gamma+1}{\gamma-1}} \right]^{1/2}$$

$$\text{else} \tag{6}$$

$$\dot{m}_i = C_{d_i} \eta_i A_i P_{0_2} \left[\frac{\gamma}{RT_0} \left(\left(\frac{P_i}{P_{0_2}} \right)^{\frac{2}{\gamma}} - \left(\frac{P_i}{P_{0_2}} \right)^{\frac{\gamma+1}{\gamma}} \right) \right]^{1/2}$$

where P_i is the static inlet pressure, A_i is the inlet area, and R is the gas constant. The conditional statement evaluates the total pressure ratio at the inlet to determine if the flow is choked. A slight improvement to the conditional statement would be to use the local static pressure upstream of the inlet, rather than the total pressure. The current formulation assumes that the inlets are located far enough forward to the nose of the vehicle that the two pressures are reasonably close.

The mass flow rate is assumed to be proportional to the isentropic flow rate, where the constant of proportionality is the product of the inlet efficiency parameter, η_i, and the discharge coefficient, C_{di}. For the inlets, the value of the discharge coefficient is taken to be that of a sharp-edged orifice, for which a curve fit was made from data available in Reference [5]. The curve fit is as follows:

$$C_{d_i} = 0.4861\left(\frac{P_i}{P_{0_2}}\right)^3 - 0.8274\left(\frac{P_i}{P_{0_2}}\right)^2 + .0992\left(\frac{P_i}{P_{0_2}}\right) + 0.85 \quad (7)$$

The inlet efficiency parameter is a function of how the inlet is made and what the shape is. From Reference [6], an η_i value of 0.7 is recommended for a cloth inlet like that used for an attached isotensoid.

Canopy Porosity Flow Rate—Calculating the mass flow rate out of the canopy due to porosity, $\dot{m}_o$, is performed in a manner similar to that for the inlets, though without the inlet efficiency parameter.

$$\text{if} \quad \frac{P_b}{P_i} \le \left(1+\frac{\gamma-1}{2}\right)^{\gamma/(1-\gamma)}$$

$$\dot{m}_o = C_{d_o} A_{base} P_i \left[\frac{\gamma}{RT_0}\left(\frac{2}{\gamma+1}\right)^{\frac{\gamma+1}{\gamma-1}}\right]^{1/2} \quad (8)$$

else

$$\dot{m}_o = C_{d_o} A_{base} P_i \left[\frac{\gamma}{RT_0}\left(\left(\frac{P_b}{P_i}\right)^{\frac{2}{\gamma}} - \left(\frac{P_b}{P_i}\right)^{\frac{\gamma+1}{\gamma}}\right)\right]^{1/2}$$

where A_{base} is the surface area of fabric located in the SIAD base. The discharge coefficient in Equation 8 is a function of the porosity of the material and the pressure differential between the internal pressure and the base pressure of the SIAD. Values of the discharge coefficient will be dependent on the type of material used and the degree to which the material was made non-porous (e.g. through coating or calendaring). To provide insight into a range of values typical for an isotensoid, data was extracted from Reference [7] for the permeability of an isotensoid model at a range of differential pressures. The data is originally provided as a measure of permeability in units of $ft^3/min/ft^2$ across a range of pressures and fabric coating levels. Using information in the Reference, a value of the discharge coefficient was backed out using Equation (8) and is shown plotted in Figure 3. The data was fitted using an equation of the following form:

$$C_{d_o} = a\exp\left[b(P_i - P_b)\right] + c\exp\left[d(P_i - P_b)\right] \quad (9)$$

Values of the coefficients for each of the three variants of models tested are provided in Table 2. It is worth noting that none of the intercepts for the curve fits passes through zero for a zero pressure differential. This is considered an artifact of the fitting process and represents a conservative approach for estimating the material porosity. One approach to modeling the porosity would be to assume that the canopy is sufficiently coated so as to be essentially non-porous. The values of porosity for the "model as fabricated" case are considered to be conservatively high for a modern day isotensoid.

Table 2 – Curvefit coefficients for the canopy discharge coefficient data shown in Figure 1.

	Model As Fabricated	Equator and Gore Seams Coated	Model Completely Coated
a	6.365E-04	1.210E-05	2.628E-04
b	6.907E-06	-9.989E-05	5.983E-06
c	-1.964E-04	3.620E-04	-7.003E-05
d	-2.423E-04	7.810E-06	-1.127E-04

Pressure Rise Calculations—Using Equations (6) and (8), a net mass flow rate into the SIAD can be calculated as:

$$\dot{m}_{net} = \dot{m}_i - \dot{m}_o \quad (10)$$

Between the time at which the inlets are exposed to the freestream, t_{if}, and the time at which the SIAD achieves full volume, t_{fv}, the inflation process is considered to occur at a constant pressure. During this time, the rate of increase in volume is calculated as:

$$\frac{dV}{dt} = \frac{\dot{m}_{net}RT_0}{P_i} \quad (11)$$
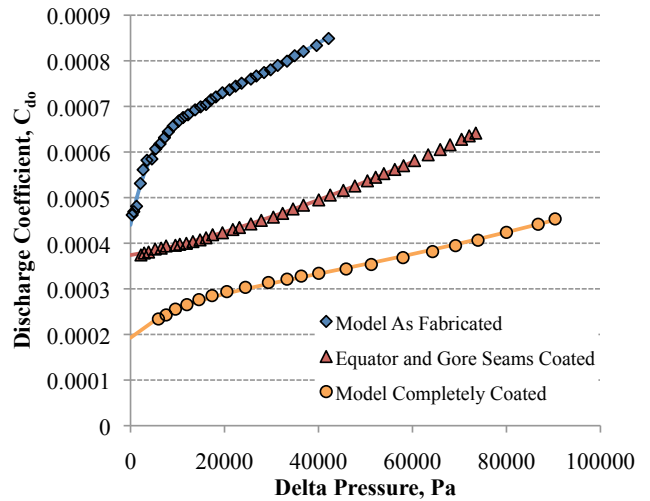
Figure 3 – Values of material porosity in the form of a calculated discharge coefficient for a Viton coated Nomex isotensoid model. Symbols correspond to the data while solid lines are a fit of the data.

Once the IAD has achieved the full volume, the pressure begins rising. During this time, the rate of increase in pressure is calculated as:

$$\frac{dP_i}{dt} = \frac{\dot{m}_{net}RT_0}{V} \quad (12)$$

Drag Area Model

Predicting the drag that is produced by the isotensoid during the inflation process is difficult due to the stochastic

4

element of ram-air inflation. Thus, a simple model is suggested that tracks the rise in drag area as proportional to the rise in internal pressure:

$$C_D A = \left(C_D A\right)_{aeroshell} + \frac{P_i}{P_{0_2}}\left[\left(C_D A\right)_{IAD} - \left(C_D A\right)_{aeroshell}\right] \quad (13)$$

where the subscript "aeroshell" refers to the drag area of the entry vehicle without the IAD deployed and the subscript "IAD" refers to the drag area of the vehicle with a fully deployed IAD. The basis for this model comes from Reference [8], where traces of internal pressure and drag force produced during inflation are shown to be very similar in shape.

Model Validation

An attempt to validate the proposed inflation and drag area models was made using wind tunnel data provided in the references. Specifically, References [4] and [8] provide internal pressure and drag force traces versus time that are used to compare against.

*Internal Pressure Calculations—*The first comparison is made using data from Reference [8], for which the results are shown in Figure 4. It should be noted that the calculated pressures were shifted in time to correspond to the inlets being exposed to the freestream. From Figure 4, it can be seen that the model does a good job of matching the rapid increase in inflation pressure that occurs once the inlets are exposed to the freestream.
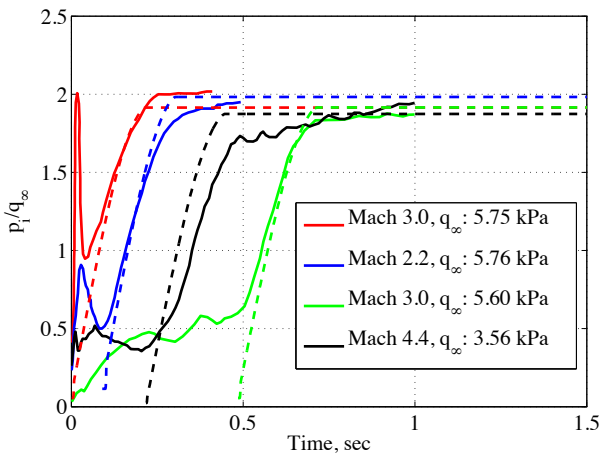
Figure 4 – Inflation model comparison with data from Reference [8]. Solid lines correspond to wind tunnel data while dashed lines are predictions from the current inflation model.

Shown in Figure 5 are comparisons with measurements provided in Reference [6]. As with the previous comparisons, these are also seen to match well with the wind tunnel measurements. Additionally, the final pressure values are seen to match with wind tunnel measurements.

These results, though limited, provide some confidence in the current inflation model.
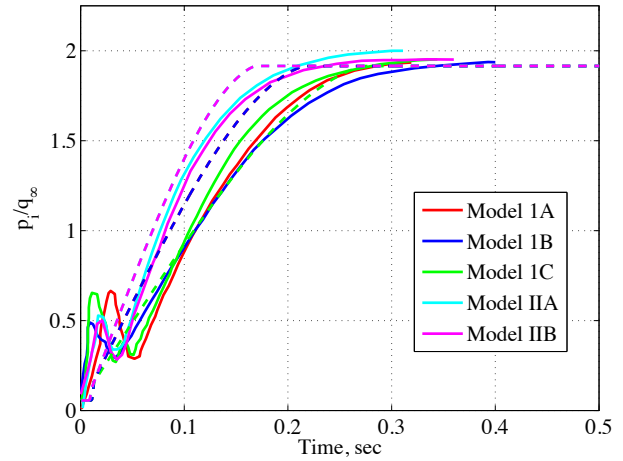
Figure 5 – Inflation model comparison with the data from Reference [4] (Mach 3, q_∞ = 5.75 kPa). Solid lines correspond to wind tunnel measurements while dashed lines are predictions from current inflation model.

Drag Area Model— Comparisons of the proposed drag area model with drag forces produced during testing are shown in Figure 6. Though simplistic in nature, the drag area model sufficiently captures the rise in average drag force.
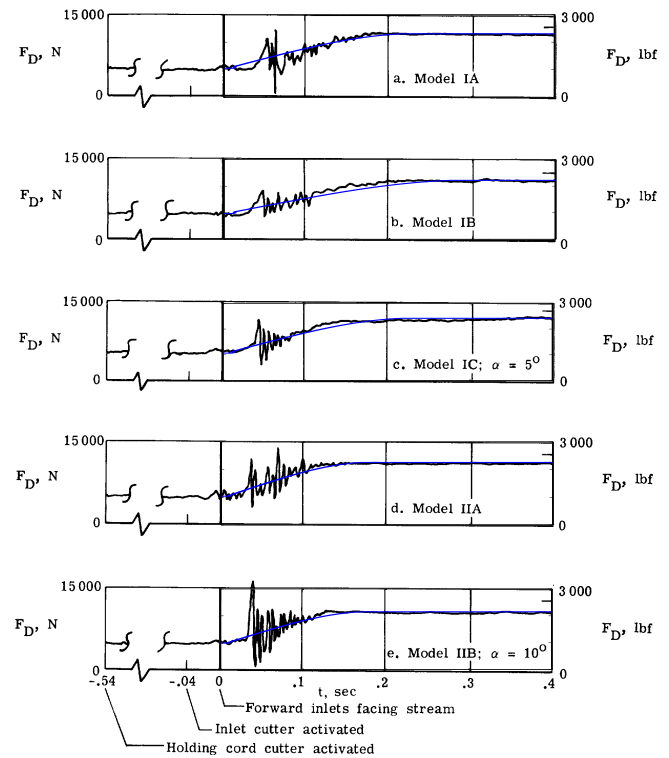
Figure 6 – Drag force rise versus time comparisons with Reference [4]. The solid blue lines correspond to drag forces predicted with the current model.

4. AEROTHERMAL MODEL AND ANALYSIS

Performing a thermal analysis of candidate IAD materials requires an input heating distribution. As was done in previous works [9], this heating distribution was calculated using axisymmetric boundary layer relations. These relations in turn required the flow conditions at the edge of the boundary layer. Thus, a basic procedure was established whereby a surface pressure distribution was computed and subsequently used as the boundary layer edge pressure distribution. Isentropic flow relations were used to solve for other necessary flow parameters at the boundary layer edge (again using the computed pressure distribution).

Aerodynamics

To compute the input pressure distribution, two separate methods were considered suitable for the engineering level analyses desired. These included a modified Newtonian analysis and an inviscid CFD analysis. Modified Newtonian aerodynamics assumes a simple impact-based model to compute a pressure coefficient as a function of the incidence angle between the surface and the freestream. It is equated as:

$$C_P = C_{P\max}\sin^2\theta = \frac{\gamma+3}{\gamma+1}\left(1 - \frac{2}{M_\infty^2(\gamma+3)}\right)\sin^2\theta \quad (14)$$

where θ is the incidence angle. The 2nd approach consisted of computing a pressure distribution using a rapid, axisymmetric Euler analysis. Using a Georgia Tech developed Cartesian grid CFD code, NASCART-GT, solutions were computed at the nominal Mars flight conditions. A comparison of the pressure distributions calculated using the two methods is shown in Figure 7.
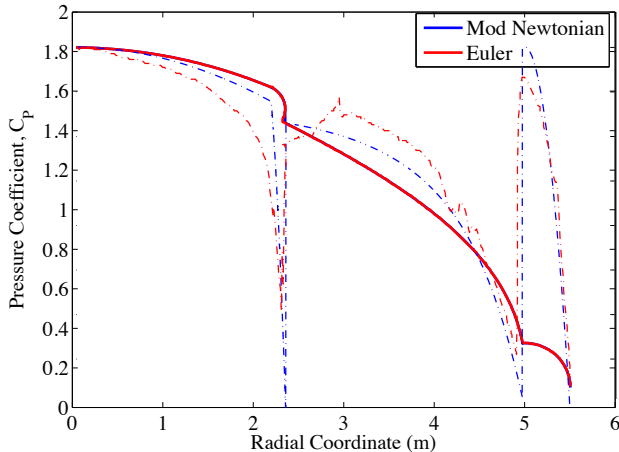
Figure 7 – Pressure coefficient computed using two methods.

As can be seen, the modified Newtonian distribution shows good agreement with the inviscid solution. The agreement is, in some places, coincidentally good because modified Newtonian does not actually model any of the physical processes. For example, the transition between the aeroshell

and isotensoid likely exhibits a small recirculation region due to the backward facing step. In the inviscid solution, a drop in pressure is observed. The modified Newtonian solution shows the same behavior, but only because the geometry is oriented parallel to the freestream (thus yielding a value of zero for the pressure coefficient). Additionally, both solutions show strong pressure rises in the vicinity of the burble fence. For the inviscid solution this is due to the presence of a weak shock in front of the burble fence, as shown in Figure 8. The modified Newtonian solution captures the pressure rise due to the burble fence having a large portion of the geometry being normal to the freestream. Because of the simplicity and good agreement with inviscid solutions, subsequent analyses utilized a pressure distribution calculated from modified Newtonian impact theory.
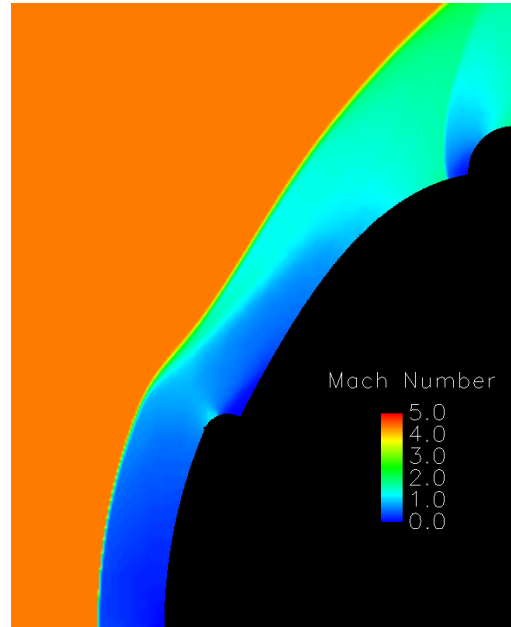
Figure 8 – Inviscid NASCART-GT solution at the nominal Mars deployment condition.

Aerothermodynamics

Calculation of a laminar and turbulent heat rate on the IAD follows the approach used by Faurote and Burgess [9], which used relations derived from axisymmetric boundary layer theory. The laminar form of the relations were originally derived by Lees [10]. The turbulent boundary layer heat transfer is calculated using the method of Rose, Probstein, and Adams [11] (again using the approach outlined in Reference [9]).

Validation

There is limited aerothermal data available on an attached isotensoid geometry and so validation of the discussed approaches is difficult. There is no free-flight data available and only one wind tunnel test was conducted for the purpose of assessing aerothermal response [12]. That test was conducted at Mach 8 on temperature sensitive material to

yield heat transfer coefficients. Though data reduction was noted to be difficult, and no uncertainties were provided, an attempt at matching the results from that test shows generally good agreement (Figure 9). The heat transfer coefficient, h_c, is shown normalized with that at the stagnation point. Two areas where the predictions differ are the stagnation region and the burble fence location, two regions where the utilized methods are less likely to be valid. The boundary layer relations utilized consistently over-predict heat rates in the stagnation region due to a denominator that goes to zero near the stagnation region. As noted previously, the burble fence region exhibits a weak shock and a small recirculation region that is less suitable for thermal analysis using boundary layer relations.
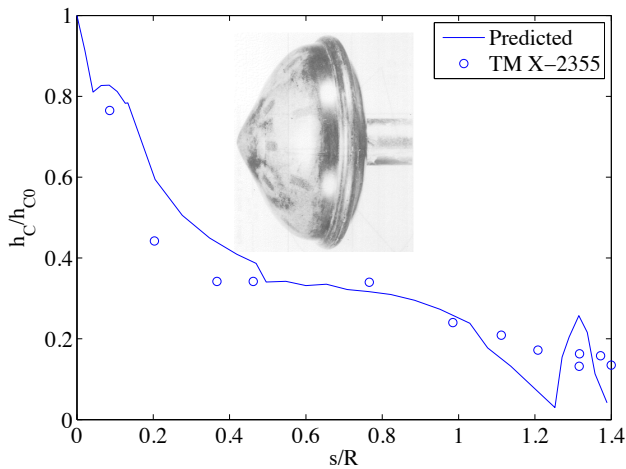

Figure 9 – Comparison of heat transfer coefficient with measured data from Ref. [12].

Results

Using the methods outlined previously, an aerothermal analysis of the attached isotensoid was conducted at three distinct Mach numbers and Mars altitudes. These flow conditions are coincident with the deployment conditions outlined in the reference mission section of this paper. Heating results are shown in Figure 10 for both laminar and turbulent flow solutions with the start of the dashed line indicating the predicted transition to turbulent flow. It should be noted that for the subsequent aerothermal analysis, it is the region of the isotensoid between the aeroshell interface and the burble fence that is of most interest. That is, although increased heating in the region of the burble fence is very likely, the values predicted by the boundary layer methods are not considered valid.

Although the boundary layer is expected to be turbulent in the region of the isotensoid between the aeroshell interface and the burble fence, the laminar solutions show a relatively higher heat rate in these regions. The condition for transition to turbulence is difficult to predict with confidence (Reynolds number of 200,000 based on running length is used here), so isotensoid aerothermal design conditions are taken from the more conservative laminar solutions. The

heating results show that, even in the most severe deployment conditions considered in this study, the peak convective heat rate is below 1.25 W/cm^2. Thermal analysis of the isotensoid fabric assumes this conservative value of heating occurs immediately after inflation and tapers off according to the ballistic trajectory. The heating boundary condition used for thermal analysis is shown in Figure 11.
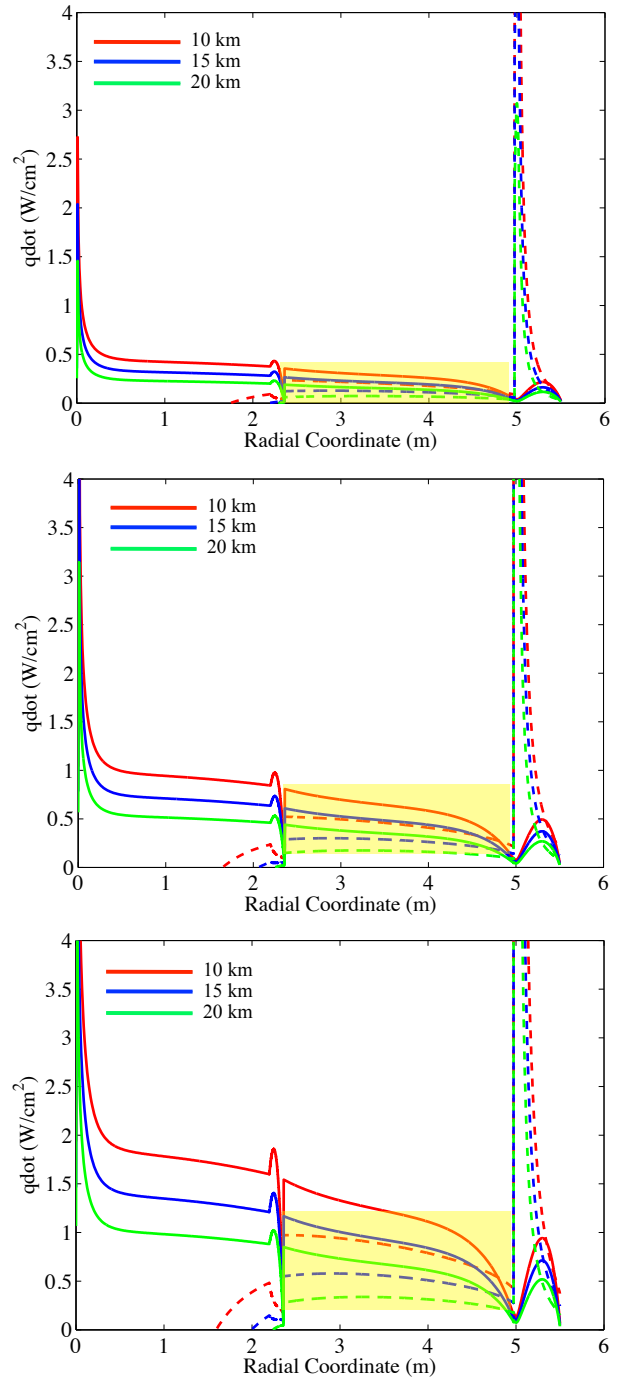
Figure 10 – Heating results for Mach 4 (top), Mach 5 (center), and Mach 6 (bottom). Dashed lines indicate turbulent solutions. The isotensoid region between the aeroshell interface and burble fence is shaded.
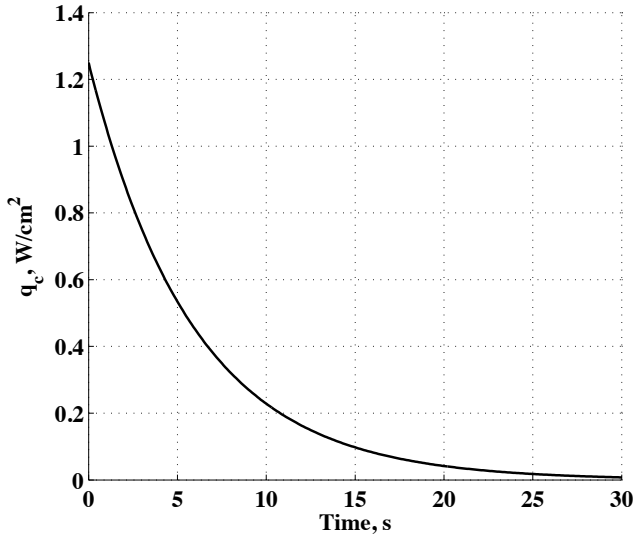
Figure 11 – Heating boundary condition.

5. THERMAL MODEL

Selecting suitable SIAD materials requires understanding of the thermal environment throughout the envelope. The transient temperature response within the multi-material SIAD envelope, $T(x,t)$, is computed with one-dimensional heat conduction relations [13]. Three material layers are considered: an outer layer of elastomeric coating, the structural fabric, and an inner layer of elastomeric coating. Figure 12 shows the three material layers and the discretization scheme.
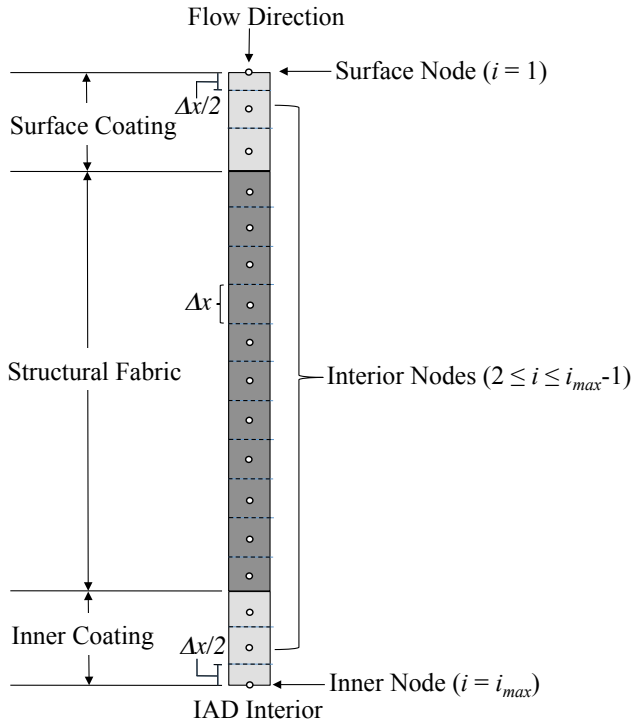

Figure 12 – Notional discrete model of three-layer IAD envelope.

The material "stack" is discretized into a surface node, several interior nodes, and an inner node. Nodes are uniformly spaced according to the total thickness of the material stack and the chosen number of nodes, $i_{max} = 50$. In order to maintain uniform node spacing, the surface and inner nodes are assigned thickness $\Delta x/2$ and the interior nodes are assigned thickness Δx (see Figure 12). Nodal energy balance equations are derived and explicitly solved for nodal temperatures using a time-marching numerical scheme. The following discussions derive expressions for the nodal temperatures through the thickness as a function of time.

Surface Node

The energy balance at the surface node is given by the model below and Equation (15):

Convective heating from boundary layer	−	Radiation into space from surface	−	Heat conducted away from outer slab	=	Heat stored in outer slab

$$\dot{q}_c - \varepsilon\sigma\left(T_1^{4n} - T_\infty^{4n}\right) - C_1\left(T_1^n - T_2^n\right) = \frac{\rho c_p \Delta x}{2\Delta t}\left(T_1^{n+1} - T_1^n\right) \tag{15}$$

where $\dot{q}_c$ is the convective heating from the boundary layer, ε is the coating emissivity, σ is the Stephan-Boltzmann constant, ρ is the fabric density, and c_p is the fabric specific heat at node 1. The term ρc_p is often referred to as the material thermal mass. The temperature notation is as follows: T_1^{4n} refers to the temperature at node 1 to the fourth power at the nth timestep, T_1^{n+1} refers to the temperature at node 1 at the $n^{th} + 1$ timestep, and so forth. The conductance term, C_1, is a function of the material properties and the current and neighboring nodes:

$$C_1 = \left(\frac{\Delta x/2}{k_1} + \frac{\Delta x/2}{k_2}\right)^{-1} = \frac{2}{\Delta x}\left(\frac{1}{k_1} + \frac{1}{k_2}\right)^{-1} \tag{16}$$

Equation (16) is applicable to multi-material layups because it ensures energy conservation between adjacent nodes with different material properties. This can be the case at the surface node when the thickness of the surface coating is much smaller than the thickness of the structural fabric. Equation (15) can be solved for the surface temperature at timestep $n + 1$:

$$T_1^{n+1} = T_1^n + \frac{2\Delta t}{\rho_1 c_{p_1}\Delta x}\left[\dot{q}_c - \varepsilon_1\sigma\left(T_1^{4n} - T_\infty^{4n}\right)\right.$$
$$\left. - \frac{2}{\Delta x}\left(\frac{1}{k_1} + \frac{1}{k_2}\right)^{-1}\left(T_1^n - T_2^n\right)\right] \tag{17}$$

Interior Nodes

The temperature in the interior nodes is computed by discretization of the 1-D heat equation:

$$\frac{\partial T}{\partial t} = \alpha \frac{\partial^2 T}{\partial x^2} \quad (18)$$

where $\alpha = k/(\rho c_p)$ is the thermal diffusivity, and k is the thermal conductivity. Discretizing Equation (18) and rearranging yields an expression in the form of an energy balance:

Energy transferred from slab i-1	$-$	Energy transferred to slab i+1	$=$	Energy added to slab i over time Δt

$$\Delta t C_{i-1}\left(T_{i-1}^{n} - T_i^{n}\right) - \Delta t C_{i+1}\left(T_i^{n} - T_{i+1}^{n}\right) = \\ \rho_i c_{pi} \Delta x \left(T_i^{n+1} - T_i^{n}\right) \quad (19)$$

where the conductance terms are

$$C_{i-1} = \frac{2}{\Delta x}\left(\frac{1}{k_{i-1}} + \frac{1}{k_i}\right)^{-1} \quad (20)$$

$$C_{i+1} = \frac{2}{\Delta x}\left(\frac{1}{k_{i+1}} + \frac{1}{k_i}\right)^{-1} \quad (21)$$

Rearranging Equation (19) and substituting the conductance terms yields an expression for the temperature of the interior nodes at timestep n+1:

$$T_i^{n+1} = T_i^{n} + \frac{\Delta t}{\rho_i c_{p_i} \Delta x}\left[\frac{2}{\Delta x}\left(\frac{1}{k_{i-1}} + \frac{1}{k_i}\right)^{-1}\left(T_{i-1}^{n} - T_i^{n}\right)\right. \\ \left. - \frac{2}{\Delta x}\left(\frac{1}{k_{i+1}} + \frac{1}{k_i}\right)^{-1}\left(T_i^{n} - T_{i+1}^{n}\right)\right] \quad (22)$$

Inner Node

The supersonic attached isotensoid is inflated by ram-air entering through inlets located on the front of the fabric envelope. The air entering the inlets quickly slows down and the isotensoid internal temperature approaches the freestream stagnation temperature. Thus, heat is transferred from the stagnant air inside the SIAD envelope to the inside surface of the isotensoid envelope by free convection [9]. Heat transfer due to free convection at this surface is much lower than the conductive heat transfer from inside the canopy, so an adiabatic boundary condition is applied to the inner wall [14][15]. An equation for the inner node temperature can be found by omitting convective heating and radiation terms from the energy balance:

$$T_{i\max}^{n+1} = \frac{4\Delta t}{\rho_{i\max} c_{p_{i\max}} \Delta x^2}\left(\frac{1}{k_{i\max-1}} + \frac{1}{k_{i\max}}\right)^{-1}\left(T_{i\max-1}^{n} - T_{i\max}^{n}\right) \\ + T_{i\max}^{n} \quad (23)$$

It is worth noting that some other configurations of attached SIADs have base surfaces that are mostly exposed to free space [16]. It is possible that these configurations could see reduced fabric temperatures as a result of re-radiation into space from the SIAD base. Note that radiation due to a non-zero view factor will influence radiative heat transfer at the SIAD base. For instance, the aeroshell base will radiate heat onto the SIAD base, and the SIAD base will radiate heat onto itself. For completion, the equation for the inner node temperature accounting for re-radiation with a view factor of zero is given by Equation (24):

$$T_{i\max}^{n+1} = \frac{2\Delta t}{\rho_{i\max} c_{p_{i\max}} \Delta x}\left[\frac{2}{\Delta x}\left(\frac{1}{k_{i\max-1}} + \frac{1}{k_{i\max}}\right)^{-1}\left(T_{i\max-1}^{n} - T_{i\max}^{n}\right)\right. \\ \left. - \varepsilon_{i\max}\sigma\left(T_{i\max}^{4n} - T_\infty^{4n}\right)\right] + T_{i\max}^{n} \quad (24)$$

Choice of Timestep

The nodal temperature expressions derived in this section rely on finite difference expressions to approximate terms in a partial differential equation. It is necessary to choose a value of Δt that ensures the time marching scheme is numerically stable. That is, we must ensure that spontaneous numerical errors do not grow as calculations proceed. The stability criterion for this numerical scheme is dependent on the value of the Fourier number, F:

$$F = \frac{\alpha \Delta t}{\Delta x^2} \quad (25)$$

For unconditional stability, the Fourier number must be set such that $0 \leq F \leq 0.5$. Tannehill shows that the numerical error of this scheme is minimized when F = 1/6 [17]. Thus, the timestep used in evaluating Equations (17), (22), and (23) is chosen to be:

$$\Delta t = \frac{\rho c_p \Delta x^2}{6k} \quad (26)$$

Note that Equation (26) is material-dependent. The worst-case timestep (lowest Δt) for a given material stack is used globally for this analysis.

Thermal Model Validation

Two validation approaches ensure that the thermal model is producing physical results. First, the analytic solution to Equation (18) for a 1-D semi-infinite conductor with constant heat rate applied to the x = 0 boundary is given by Equation (27).

$$T(x,t) = T_i + \frac{2\dot{q}_c(\alpha t/\pi)^{0.5}}{k}\exp\left(-\frac{x^2}{4\alpha t}\right) - \frac{\dot{q}x}{k}erfc\left(\frac{x}{2\sqrt{\alpha t}}\right) \quad (27)$$

where $erfc$ refers to the complementary error function. The simple explicit scheme described in this section should produce a solution identical to Equation (27) as the timestep, ΔT, approaches zero. Figure 7 shows a comparison

of the simple explicit scheme and Equation (27) for copper and a constant heat flux of 30 W/cm^2. The numerical error between the simple explicit result and the analytic result is less than 2% for the stated Fourier number criterion.
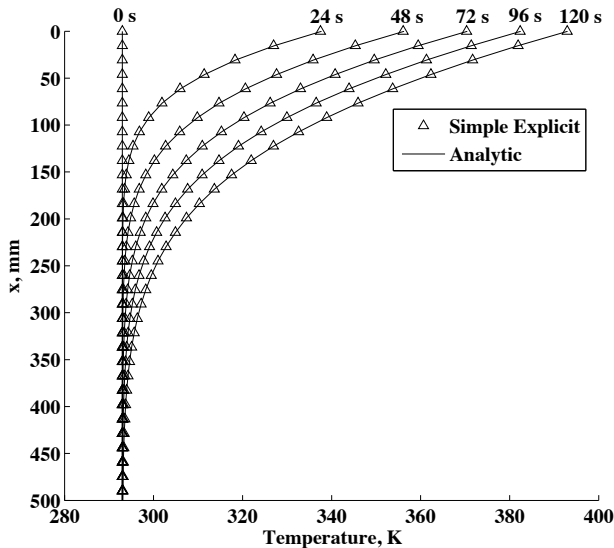
Figure 13 – Comparison of simple explicit scheme and analytic solution for a semi-infinite copper conductor.

The second validation approach seeks to verify the multi-material capability of the simple explicit scheme. In order to ensure that energy is being conserved throughout deceleration, the net heat flux is integrated to provide the history of energy added and removed from the SIAD envelope. This quantity is shown to be identical to the sum of the nodal energy throughout the envelope at a given time. The heat flux and energy are shown in Figure 14 for a Vectran isotensoid envelope with initial heat flux of 2 W/cm^2. The energy is added and removed from the system as expected. These validations provide confidence in the corresponding temperature solutions described later in thermostructural analysis section of this paper.
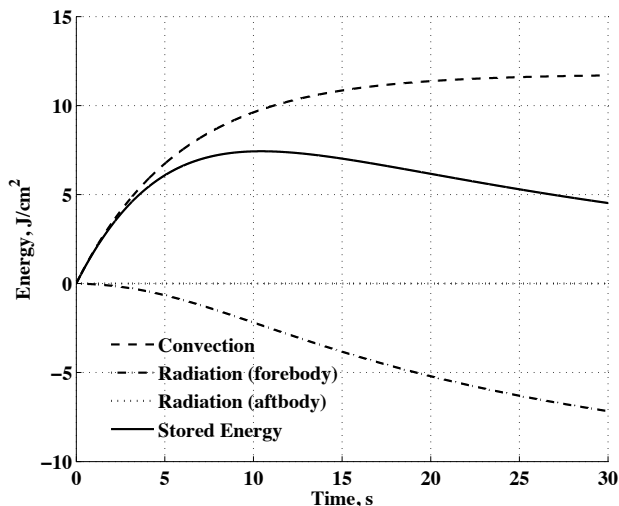

Figure 14 – Energy added and removed from IAD canopy is equivalent to the stored energy.

6. CANDIDATE MATERIALS

Bulk mechanical and thermal properties of the fabrics considered in this study are provided in Table 3. Properties of Viton elastomeric coating (thermal protection and porosity reduction) are also shown. Modern SIADs have often been coated with urethane- or silicon- based coatings, but only Viton is considered in the present analysis for the sake of brevity. The thermal model described earlier in this paper showed heat flux due to thermal radiation is a cooling mechanism directly proportional to the thermal emissivity of the coating, ε. The precise value of Viton coating emissivity is not well understood (a nominal value of 0.85 is assumed), so a sensitivity study is presented later to help resolve the sensitivity of peak fabric temperature to this parameter.

The state-of-the-art fabrics in the 1960s were constructed from flexible-chain polymer fibers such as Nomex, nylon, and Dacron. Nomex was chosen for the majority of the SIAD test articles in this era due to superior strength retention under prolonged thermal and structural loading. Manufacturing flexible-chain polymers in a way that maximizes their tensile strength requires that the fibers be mechanically drawn out in the solid phase. This process limits the fibers from reaching their theoretical maximum tensile strength. Additionally, flexible-chain polymers tend to associate in random orientations when concentration is increased, further complicating the process of fiber alignment [18].

Modern day materials under consideration for SIADs are comprised of rigid-chain "rod-like" polymers rather than flexible-chain polymers. In contrast to the historical fiber materials, rigid-chain polymers tend to align parallel to one another as concentration increases, thus increasing the tenacity of the fiber. Furthermore, the fiber orientation process of rigid-chain polymers can be achieved in the liquid state facilitating formation of fully-extended chains. Figure 15 shows a schematic of the polymer structure for flexible and rigid polymers during the manufacturing process.
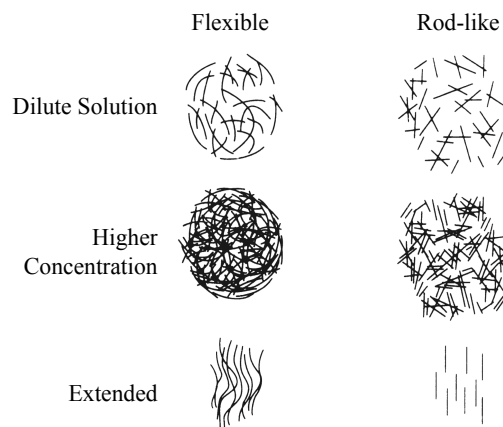
Figure 15 – Differences between flexible and rigid polymers during manufacturing (adapted from [18]).

Table 3 – Tensile and thermal properties of candidate SIAD materials fabrics. Properties for a Viton coating are also shown.

Material	Thickness (mm)	Tensile Strength (MPa)	Density (kg/m^3)	Areal Density (kg/m^2)	Specific Heat (J/kg-K)	Thermal Conductivity (W/m-K)	Reference
Nomex	0.203	600	384	0.0780	1465	0.035	[9]
Kevlar	0.127	3600	1440	0.1829	1420	0.04	[18]
Vectran	0.127	3000	1400	0.1778	1259	0.37	[19]
Viton	Variable	--	1842	Variable	1654	0.202	[9]

Kevlar and Vectran, both rigid-chain polymers, are two of the materials under consideration as SIAD fabrics. Both materials have performed successfully as inflatable structures in flight projects. Kevlar was used as the structural fabric for the NASA Langley Inflatable Reentry Vehicle Experiment (IRVE), and Vectran was used for the landing airbags on Mars Pathfinder and the Mars Exploration Rovers. Kevlar was introduced in 1971 by DuPont as an answer to the difficulties of manufacturing flexible-chain polymers into maximum strength synthetic fibers. Vectran, introduced 15 years later, has similar thermal mass (ρc_p) to Kevlar but different strength retention properties. In particular, Kevlar retains more of its tenacity when operating at high temperature, but Vectran retains more of its tenacity after cooling from extended durations of thermal exposure [19]. SIADs at Mars will experience heating that may substantially reduce the tenacity of materials for a very short period of time. Tenacity retention implications for the reference mission considered in this paper are discussed later in the thermostructural analysis.

SIAD fabrics must be able to perform after storage for several months in a high-density packed state subject to launch vibrations, so abrasive properties are an important consideration in this application. Vectran has been shown to have far greater resistance to abrasion and compression fatigue than Kevlar [19]. In an abrasion test of fibers for marine applications, the Vectran fibers formed "kink bands" with the number of kink bands increasing with increasing number of cycles. The energy absorbed in formation of these kink bands appeared to provide nearly five times the resistance to failure during flex folding over aramid fiber (Kevlar) [19]. These tests investigated failure due to abrasion after repeated use, so it is not clear if these results can be used to fairly discriminate potential SIAD materials. Nevertheless, it is clear that the performance of the fiber microstructure must be considered at the same importance of bulk mechanical and thermal properties when selecting a suitable SIAD fabric.

7. THERMOSTRUCTURAL ANALYSIS

Modeling the physics of IAD fluid-structure interaction is an emerging area of research and is necessary for understanding the stress distribution in the materials. Various degrees of numerical coupling are used to simultaneously solve the partial differential equations that describe fluid motion and composite material deformation. Current methods employ high-performance computers and

can be cumbersome to setup. The present analysis provides an engineering-level estimate of the fabric and meridional cord stress using isotensoid theory. The results are used to select suitable fabric thicknesses, which are then subject to thermal analysis. Nomex, Kevlar, and Vectran materials are considered.

Structural Analysis

The isotensoid shape developed in Reference [20] is a result of prescribing equal principal membrane forces in the fabric envelope and solving the governing structural equations. Obtaining the design shape requires iteratively solving the governing structural equations and computing the surface pressure profile until convergence. However, fabric and meridian stresses can be computed more directly and without iteration. Reference [21] provides normalized formulae for the meridian tension, T_r, and fabric stress, f_r, in the material located behind the burble fence (the aft chord from Point B to Point F in Figure 2):

$$T_r = \bar{T}_r \frac{P_{ref} \pi R^2}{n} \tag{28}$$

$$f_r = \bar{f}_r \frac{P_{ref} R}{2} \tag{29}$$

where $\bar{f}_r$ and $\bar{T}_r$ are non-dimensional shape parameters, P_{ref} is the difference between the internal pressure and the base pressure, R is the equatorial radius not including the burble fence (5 m), and n is the number of meridians. The isotensoid shape parameters are given in Table 4.

Table 4 – Isotensoid shape parameters.

Parameter	Value
$\bar{f}_r$	0.1100
$\bar{T}_r$	0.3812
n	48

Meridian tension and fabric stress in the front envelope (Point A to Point B in Figure 2) must account for the discontinuous load imparted by the burble fence, N_b:

$$T_f = \gamma T_r \tag{30}$$

$$f_f = \gamma f_r \qquad (31)$$

where

$$\gamma = 1 + \frac{\beta}{1 - \alpha^2} \qquad (32)$$

and

$$\beta = \frac{N_b}{P_{ref} \pi R^2}, \qquad \alpha = \sqrt{1 - f_r - T_r} \qquad (33)$$

Note that γ is strictly greater than one, so the front fabric stress and meridian tension will be greater than the rear values. Equations (30) and (31) show that the peak stresses occur when the value of internal pressure is the highest. It was shown in the inflation analysis section of this paper that the internal pressure is directly proportional to the freestream dynamic pressure, so we can fairly assume that the peak stresses will occur at the full pressure time, t_{fp}. The burble fence load, N_b, at time t_f is computed using modified Newtonian flow theory for a half-torus as 80.8 kN.

Predicted meridional cord loads and fabric stresses for the three minimum gauge materials considered are shown in Table 5. The safety factor is the ratio of the material tension strength to the computed fabric stress. For the meridians, a cord diameter of 1 cm is assumed for the safety factor calculation. These results indicate that minimum gauge materials are more than capable of handling the maximum fabric stresses in the isotensoid. Additionally, meridional cords can be constructed of the same material as the envelope fabric with plenty of margin from failure. Thus, the material sizing shown in Table 3 is assumed in subsequent thermal analyses.

Table 5 – Maximum fabric stresses and safety factors for candidate SIAD materials. Cord safety factor assumes a 1 cm diameter meridian.

Material	Tensile Strength (MPa)	Cord Load (N)	Cord Safety Factor	Fabric Stress (MPa)	Fabric Safety Factor
Nomex	600	5972	8	13	46
Kevlar	3600	5972	47	21	174
Vectran	3000	5972	39	21	145

Thermal Analysis

Structural analysis shows that minimum gauge materials can perform suitably, so the temperature history of the canopy can now be computed using the thermal model discussed earlier. It is of primary interest to deduce whether or not the fabric temperature will exceed the thermal capability of the stressed materials. Also of interest is the sensitivity of the temperature results to different thicknesses of elastomeric

coating. Understanding this relationship informs parametric SIAD mass models requiring coating thickness as an input.

The maximum temperature in the fabric as a function of thermal coating density is shown in Table 6. Note that adding a modest amount of coating can greatly reduce peak temperatures. This addition adds thermal mass, ρc_p, to the material stack and effectively raises the amount of energy required to increase the fabric temperature.

To better visualize the effect of increasing the coating thickness, the Vectran fabric temperature histories for three coating thicknesses is shown in Figure 16. It is evident that adding additional coating both reduces the peak temperature and slows the process of temperature change.

**Table 6 – Maximum fabric temperatures for different Viton coating thicknesses.**

Thermal Coating Areal Density (ozm/yd^2)	Fabric Temperatures (K)		
	Nomex	Kevlar	Vectran
1	489	435	446
3	444	411	418
6	407	387	391
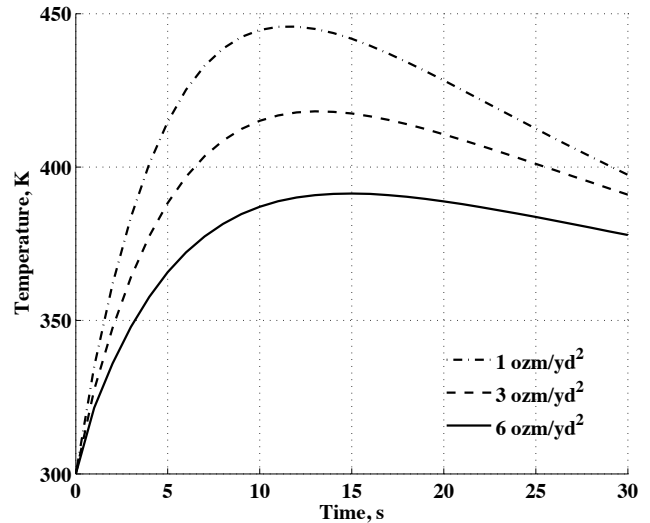
Figure 16 – Vectran temperature histories for different amounts of Viton outer coating.

The thermal mass effect can also be seen by comparing the temperature histories of the three materials for a fixed fabric thickness, as shown in Figure 17. Kevlar has approximately 16% higher ρc_p than Vectran, and Nomex has approximately 68% lower ρc_p than Vectran. A sensitivity analysis showed that the peak temperature difference can be almost entirely attributed to thermal mass differences. That is, Kevlar's relatively low thermal conductivity does not influence the peak temperature results relative to the higher thermal conductivity materials. The thickness of the SIAD envelope is so low that even a large difference in thermal

conductivity amounts to little change in the temperature results.
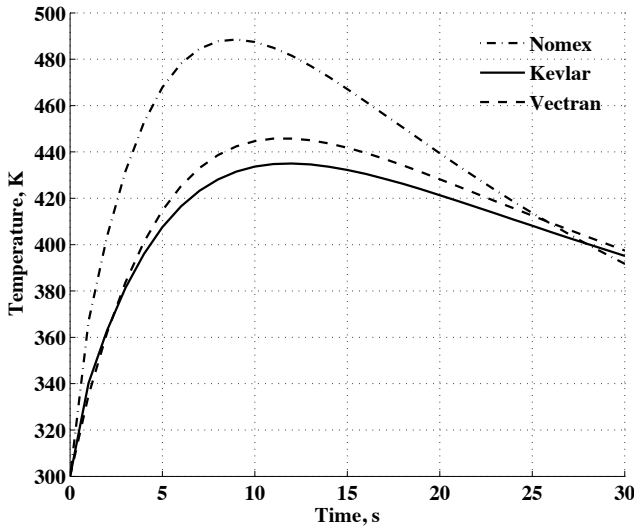
Figure 17 – Fabric temperature histories for Nomex, Kevlar, and Vectran with 1 ozm/yd^2 of Viton coating.

It is worth investigating the sensitivity of the peak fabric temperature to the peak heat rate in case future aerothermal analyses reveal less benign aerothermal environments. Figure 18 shows peak temperature results for peak heat rates as high as 3 W/cm^2 for the candidate materials. Tenacity retention percentiles are indicated with markers from the limited available data.

The results in Figure 18 show that the computed fabric temperatures for Kevlar and Vectran will result in loss of material tenacity. At the nominal convective heat rate of 1.25 W/cm^2, the tenacity retention of Vectran and Kevlar will be approximately 50% and 75%, respectively. The loss in strength due to elevated temperature is worse for Vectran than Kevlar, but this data must be considered with the results of the stress analysis. Both materials were shown to be capable of supporting the maximum stress with safety factors from material failure on the order of 100. Based on the structural margin computed for this application, the substantial reduction in tenacity retention should not necessarily disqualify either material. Furthermore, thermal exposure test data indicate that Vectran and Kevlar retain most of their tenacity once cooled from their elevated temperature. Unfortunately strength retention data after thermal exposure to Mars-relevant SIAD flight envelopes (on the order of 10-20 seconds) are not available for the candidate materials.
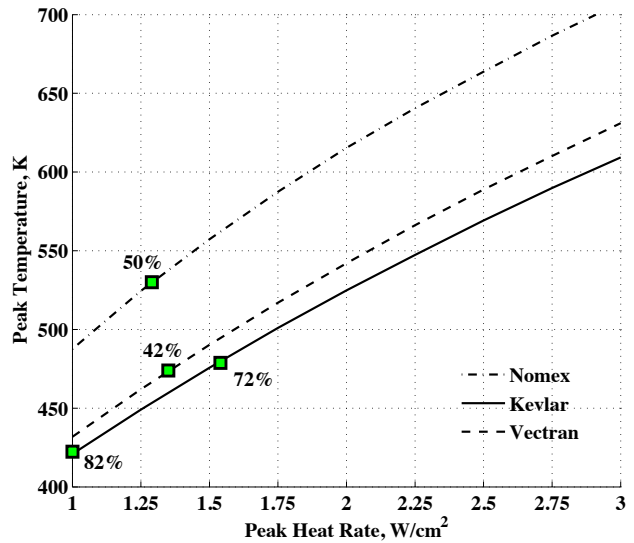
Figure 18 – Sensitivity of peak fabric temperature to peak heat rate. Markers indicate test data for tenacity retention percentile at a known temperature [9][19].

The Viton coating emissivity, ε, is not a well-understood parameter. Coating emissivity is independently varied for a nominal case in order to investigate the sensitivity of the peak temperature results to this parameter. Results for 1 ozm/yd^2 of Viton coating and Vectran fabric are shown in Table 7 for an emissivity range of 0.5 to 1. The blackbody emission case ($\varepsilon = 1$) only yields a 1.3% reduction in peak temperature. Conversely, should the Viton emit less than nominally, the peak temperature will not increase by more than 4%. This result is best explained by examining the energy added and removed from the SIAD fabric as a function of time (see Figure 14). The peak temperature is only dependent on the balance of heat flux in the first 10 to 15 seconds after SIAD inflation. During this period, the convective heat flux into the fabric (slope of the energy curves in Figure 14) is at its maximum, and the radiative heat flux out of the fabric is at its minimum. The radiative heat flux is directly proportional to the quantity $T_1^{4n} - T_\infty^{4n}$ which is minimized at time $t = 0$. Conversely, the total integrated heat load should be much more sensitive to coating emissivity than the peak temperature. However, given that these materials have proven strength retention after heat flux exposures of 24 hours, integrated heat load is not considered an important parameter in selecting SIAD materials. The peak temperature is much more dependent on the peak heat rate than the integrated heat load.

Table 7 – Sensitivity of peak fabric temperature to Viton emissivity. Nominal emissivity is 0.85 (*emphasized*).

Emissivity	% Change in ε	Peak Temperature (K)	% Change in Temperature
0.5	-41.2%	463	3.8%
0.65	-23.5%	455	2.0%
0.8	-5.9%	448	0.4%
0.85	*0.0%*	*446*	*0.0%*
1	17.6%	440	-1.3%

Of the materials considered, Vectran is recommended as an attached isotensoid SIAD envelope structure. The material has flight heritage at Mars as an inflatable structure, has favorable abrasion properties as a polymer, and can be used at minimum gauge for the expected thermostructural loads. A nominal amount of thermal protection coating should be used to reduce porosity and combat tenacity reduction at the peak fabric temperature. Material testing of stressed SIAD fabric at relevant heat rates for relevant durations is recommended prior to large-scale system tests. It is expected that unforeseen complications will arise with full-scale construction of the SIAD regardless of the choice of material. It will be impossible to manufacture the SIAD from a single sheet of fabric, so discrete gores will need to be sewn together to best match the design shape. The seams introduce ridges, regions of variable fabric thickness, and potential weakness in the envelope structure. While this study has shown the feasibility of Vectran as a SIAD material, subsequent thermostructural analyses should focus on the more pragmatic concerns of manufacturability and testability of full-scale flight articles.

8. CONCLUSION

The system-level benefits of IADs have been demonstrated through a body of literature spanning over fifty years, but only recently is the performance of relevant-scale flight articles being explored. This paper describes performance models of an attached isotensoid SIAD for use in preliminary design and describes a thermostructural analysis for a relevant mission. A model for computing the pressure and drag history of the SIAD during deployment and inflation is presented. The inflation model provides a framework for determining trajectory implications of inflation. The predicted drag force history and internal pressure profile are verified against experimental data.

Axi-symmetric boundary layer relations are presented to provide the aerothermal environment of the SIAD post-inflation. A maximum convective heat rate of 1.25 W/cm^2 for the isotensoid envelope is computed. An explicit solution to the 1-D heat transfer equations is presented for a discretized model of the multi-material SIAD envelope. Equations for the fabric temperatures as a function of time are given.

Three candidate SIAD materials are considered in this thermostructural analysis: Nomex, Kevlar, and Vectran. Nomex, the material chosen for the Goodyear SIADs during the Viking-era, is comprised of a flexible-chain polymer that cannot be manufactured to its theoretical maximum tensile strength. Kevlar and Vectran, both rigid-chain polymers, can be manufactured to achieve far greater tensile strength than historical materials. Furthermore, Vectran fibers appear more resistant to abrasion than Kevlar fibers, a key consideration in selecting suitable SIAD materials.

The thermostructural analysis is an application of the aforementioned mathematical models to the aforementioned materials. Isotensoid theory shows that all three materials can support the expected fabric stresses at their minimum gauge thicknesses. Thermal analysis of the fabrics shows that material temperatures will result in significant tenacity reduction. However, the structural margins for this application should overcome thermal weakening of the materials. Strength retention data for these materials after cooling from elevated temperature is based on heat exposure durations far longer than relevant for SIADs at Mars. A test designed to obtain strength retention data for shorter exposures to relevant heating would provide further confidence in the material performance. Vectran is recommended as the material for the SIAD due to its combination of adequate thermostructural performance, favorable abrasive properties, and flight heritage as an inflatable structure.

REFERENCES

[1] Smith, B.P., Tanner, C.L., Mahzari, M., Clark, I.G., Braun, R.D., "A Historical Review of Inflatable Aerodynamic Decelerator Technology Development," 2010 IEEE Aerospace Conference, Big Sky, MT, IEEEAC 1276, March 2010.

[2] Clark, I.G., Hutchings, A.L., Tanner, C.L., Braun, R.D., "Supersonic Inflatable Aerodynamic Decelerators for Use on Future Robotic Missions to Mars," Journal of Spacecraft and Rockets, Vol. 46, No. 2, March-April 2009, pp. 340-352.

[3] Faurote, G. L., "Design, Fabrication, and Static Testing of Attached Inflatable Decelerator (AID) Models," NASA Contractor Report CR- 111831, March 1971.

[4] Bohon, H. L., Sawyer, J. W., Miserentino, R., "Deployment and Performance Characteristics of 1.5-Meter Supersonic Attached Inflatable Decelerators," NASA Technical Note TN D-7550, June 1974.

[5] Shapiro, A. H., The Dynamics and Thermodynamics of Compressible Fluid Flow, Volume I, Ronald Press Co, 1953, pp 83-100.

[6] Bohon, H. L., Miserentino, R., "Attached Inflatable Decelerator (AID) Performance Evaluation and Mission-Application Study," Journal of Spacecraft and Rockets, Vol. 8, No. 9, August 1971, pp. 952–957.

[7] Deaton, J. W., Willis, C. M., "The Effects of Uniaxial and Biaxial Tensile Loads and Load Cycling on the Air Permeability of a Lightweight Coated Fabric," AIAA Paper 1970-1178, September 1970.

[8] Bohon, H. L. and Miserentino, R., "Deployment and Performance Characteristics of 5-Foot Diameter (1.5 m) Attached Inflatable Decelerators From Mach Number 2.2 to 4.4," NASA Technical Note TN D-5840, August 1970.

[9] Faurote, G.L., Burgess, J.L., "Thermal and Stress Analysis of an Attached Inflatable Decelerator Deployed in the Mars and Earth atmospheres," GER-14939, 1971.

[10] Lees, L., "Laminar Heat Transfer Over Blunt Bodies at Hypersonic Flight Speeds," Jet Propulsion, Vol. 26, No. 4, April 1956, pp. 259-269.

[11] Rose, P.H., Probstein, R.F., Adams, M.C., "Turbulent Heat Transfer Through a Highly Cooled, Partially Dissociated Boundary Layer," Journal of Aerospace Sciences, Vol. 25, No. 12, 1958, pp. 751-760.

[12] Creel Jr., T.R., Miserentino, R., "Aerodynamic Heating at Mach 8 of Attached Inflatable Decelerator Configurations," NASA TM X-2355, October 1971.

[13] Incropera, F.P., Dewitt, D.P., Bergman, T.L., Lavine, A.S., Fundamentals of Heat and Transfer, 6th Edition, Wiley, 2006.

[14] Nebiker, F.R., "PEPP Ballute Design and Development Fina7l Report," GER-13368, 1967.

[15] Bloetscher, F., "Aerodynamic Deployable Decelerator Performance-Evaluation Program, Phase II," GER-12907, 1967.

[16] Clark, I.G., "Aerodynamic Design, Analysis, and Validation of a Supersonic Inflatable Decelerator," PhD Thesis, 2009.

[17] Tannehill, J.C., Anderson, D.A., Pletcher, R.H., Computational Fluid Mechanics and Heat Transfer, 2nd Edition, Taylor & Francis, 1997.

[18] DuPont Advanced Fiber Systems, "Technical Guide: Kevlar Aramid Fiber."

[19] Celanese Acetate LLC, "Vectran Engineering Data," 1999.

[20] Houtz, N.E., "Optimization of Inflatable Drag Devices by Isotensoid Design," 1st Annual AIAA Meeting, Washington, DC, AIAA 64-436, June 1964.

[21] Barton, R.R., "Development of Attached Inflatable Decelerators for Supersonic Application," Goodyear Aerospace Corporation, NASA Contractor Report CR-66613, May 1968.

BIOGRAPHY

Brandon Smith is a graduate research assistant in the Space Systems Design Laboratory at the Georgia Institute of Technology. Brandon has previously interned at NASA Jet Propulsion Laboratory, NASA Langley Research Center, NASA Ames Research Center, Andrews Space, and Sikorsky Aircraft Corporation. His research has focused on technology development of supersonic and hypersonic IADs. Brandon is currently developing modeling and simulation capabilities to predict pitch oscillation for supersonic IADs at Mars. He has a BS in Aerospace Engineering from Georgia Tech and recently completed his MS in Aerospace Engineering from Georgia Tech in December 2010. He is co-advised by Dr. Robert Braun and Dr. Ian Clark.

Ian Clark is a visiting assistant professor at the Georgia Institute of Technology and an employee of the Jet Propulsion Laboratory. He received his PhD from the Georgia Institute of Technology, where he also received his BS and MS. Ian's current research involves developing and maturing IADs for use during atmospheric entry. As part of this research, Dr. Clark has worked on conceptual IAD system design, entry flight mechanics trades, and the development of fluid-structure interaction codes capable of predicting the behavior of flexible decelerators.

Robert Braun is an Associate Professor in the Daniel Guggenheim School of Aerospace Engineering at the Georgia Institute of Technology. As Director of Georgia Tech's Space Systems Design Laboratory, he leads a research program focused on the design of advanced flight systems and technologies for planetary exploration. He is responsible for undergraduate and graduate level instruction in the areas of space systems design, astrodynamics and planetary entry. Prior to coming to Georgia Tech, Dr. Braun worked at NASA Langley Research Center for sixteen years where he contributed to the design, development, test, and operation of several robotic space flight systems. Dr. Braun is an AIAA Fellow and the principal author or co-author of over 175 technical publications in the fields of planetary exploration, atmospheric entry, multidisciplinary design optimization, and systems engineering. Dr. Braun is currently serving as the NASA Chief Technologist.